© Universiti Tun Hussein Onn Malaysia Publisher's Office

IJIE

http://penerbit.uthm.edu.my/ojs/index.php/ijie
ISSN : 2229-838X e-ISSN : 2600-7916

The International Journal of Integrated Engineering

Effect of Roof Design Configurations on Natural Ventilation with an Obstacle Inside the Building Model

Lip Kean Moey[1*], Kian Shen Wan[2], Vin Cent Tai[1], Tze Fong Go[3], Perk Lin Chong[4]

[1]Centre for Modelling and Simulation, Faculty of Engineering, Built Environment & Information Technology, SEGi University, Selangor, MALAYSIA

[2]Faculty of Engineering, Built Environment & Information Technology, SEGi University, Selangor, MALAYSIA

[3]Centre for Advance Materials and Intelligent Manufacturing, Faculty of Engineering, Built Environment & Information Technology, SEGi University, Selangor, MALAYSIA

[4]School of Computing, Engineering & Digital Technologies, Teesside University, Middlesbrough, TS1 3BX, UNITED KINGDOM

DOI: https://doi.org/10.30880/ijie.2023.15.07.002
Received 14 July 2023; Accepted 3 October 2023; Available online 5 December 2023

Abstract: Roof shape, roof angle, and internal obstacle are some of the factors that have a substantial impact on building's ventilation performance. However, previous roof ventilation studies have not considered the influence of internal obstacle which can affect the overall building's ventilation performance. For this study, CFD was used to study the effect of roof design configurations on natural ventilation with an obstacle inside the building model. The numerical simulation was carried out by using steady RANS equation specifically the Standard k-ε with enhanced wall treatment. A total of 40 simulation cases were carried out. The study considered two roof shapes mainly the sawtooth roof and the saltbox roof with varying roof angle which were 10º, 20º, 30º, and 40º. Internal obstacles with various height were further added into the simulation cases. Next, grid sensitivity analysis was carried out using Grid Convergence Index (GCI) and Factor of two of observations (FAC2) analysis was carried out as model verification method to ensure a reliable simulation result. Based on the results, it is found that airflow characteristics such as wind speed, distribution of pressure coefficient, and flowrate of an isolated building are strongly dependent on the roof shape and roof angle. Next, the dimensionless flowrate (DFR) is measured to be highest with largest roof angle while lowest with smaller roof angle. Furthermore, the DFR of a building with internal obstacle is lower than that without an internal obstacle due to blockage of incoming air. Moreover, the results show that the sawtooth roof outperforms the saltbox roof in terms of measured parameter. Finally, the study concluded that an isolated building with higher roof angle and without an internal obstacle leads to the best dimensionless flowrate throughout the building.

Keywords: Natural ventilation, roof ventilation, CFD, obstacle height, dimensionless flowrate

1. Introduction

Over the last few decades, technology has been progressing at an astounding rate. Due to industrialization, human activities have significantly affected the Earth's climate, with some of these effects being temperature rise, water shortage, and reduced crop yield [1]. Therefore, to tackle this issue, low carbon and green buildings are promoted worldwide to ensure sustainability. Natural ventilation is one of the sustainable methods which makes the building

*Corresponding author: moeylipkean@segi.edu.my

more efficient and less dependent on non-sustainable resources. It is found that a good building layout design that uses natural ventilation may cut power consumption for buildings by 13% to achieve thermal comfort [2]. Moreover, ventilation allows fresh outdoor air to enter the building and replace the air currently present inside thus improving the overall air quality inside the building.

A lack of natural ventilation can cause an increase in indoor temperatures attributed to ineffective passive design in modern houses. In the design of a home, the roofing system is crucial because the roof accounts for 70% of the overall heat gain [3]. One of the common passive designs used to increase natural ventilation is through roof configuration as roof configurations and shapes can change pressure distribution and flowrate through the building [4]. Examples of common roof shapes are gable roof, venturi roof, saltbox roof, and sawtooth roof.

In recent years, more research works were carried out to study the roof configuration and its effect on natural ventilation. A study of the roof tilt angle and asymmetrical opening on the volumetric flow rate for a building was investigated [4]. Results show that the building with 45-degree roof inclination outperforms all other cases. Another study, which examined the impact of asymmetrical opening positions and sawtooth roof angles on a building [4], revealed that the highest volumetric flow rate occurs when the roof is inclined at 27-degrees and the opening is at the middle-top position. This means that the ventilation flow is dependent on the roof angle. Furthermore, research conducted by Moey et al concluded that the higher gable roof pitch increased the ventilation rate as airflow behavior and characteristics depend on the roof angle [5]. Similar results were obtained in study conducted by Tominaga et al where it was observed that the airflow pattern surrounding a building change intensely with various roof angle [7]. Moreover, both studies concluded that the critical roof angle is around 18° for gable roof whereby notable differences in airflow is observed [5].

In addition, roof configuration was found to influence natural ventilation performance wherein the airflow and pressure distribution are highly dependent on roof shapes [8]. A study on the effect of eave and roof pitch for a sawtooth roof building was investigated. The findings suggest that the building with a leeward eave angle of 90-degrees and a roof pitch of 55-degrees exhibits the most significant increase in ventilation rate, which is at 7.16% [4]. Furthermore, the previous study also concluded that the saltbox roof type performed better than the gable roof wherein the increased height of the saltbox roof increased the impinging influence on the air flow [12]. On the other hand, research was carried out on the impact of internal obstacles for a natural-ventilated building. The location and size of the obstacle was varied to measure its effect on ventilation. The study found that internal obstacle height does not affect external airflow which is outside the building as the Cp value were similar with various obstacle height. Finally, the study concluded that the effect of larger internal obstacle should be considered to prevent overestimation of ventilation performance [13]. This finding aligns with numerous previous studies, which have consistently shown that buildings with internal obstacles tend to have lower ventilation rates compared to those without such obstacles [15] .

The aforementioned studies presented above have shown that roof shape, roof angle and internal obstacle are crucial parameters that influence airflow, ventilation rate and other parameters throughout the building. To the best of authors' knowledge, previous roof ventilation studies have not considered the influence of internal obstacles which can affect the overall building's ventilation performance. Hence, this research uses CFD to study the effect of roof design configurations specifically sawtooth and saltbox roof on natural ventilation with an obstacle inside the building model.

This present study is further broken down into various sections. In section 2, information on numerical study such as simulation cases, computational domain, boundary conditions, and grid sensitivity analysis will be discussed. Additionally, section 3 will present and analyze the simulation results. Lastly, the overall research achievement will be concluded in section 4.

2. Numerical Study

2.1 Model

The building model used by van Hoff et al was selected in this study as a reference model **Error! Reference source not found.**. The building model's dimensions were 200 mm × 200 mm × 160 mm (L × W × H), which is a reduced scale of 1:100 from the full- size building. Other than that, the building has a thickness of 3 mm, and has an opening location at height of 80 mm on both windward and leeward facades. The opening is 36 mm in height and 92 mm in width, which corresponds to an area of 3.312×10^{-3} m^2 in reduced scale. Figure 1 shows the dimensions of the reference model. Moreover, 40 additional simulation cases were modified based on the reference model. The simulation cases consist of two roofs namely sawtooth roof and saltbox roof in which the roof pitches were manipulated to roof angle of 10°, 20°, 30°, 40°, with and without internal obstacles. The simulation cases also include different internal obstacle heights namely 80 mm, 100 mm, 120 mm, and 140 mm with 3mm thickness, and a fixed length L = 180 mm positioned at the center of the building model. Furthermore, a roof opening with dimensions of 92 mm × 18 mm was added which is half of the window opening size. Figure 2a and 2b show the dimensions of sawtooth roof and saltbox roof, respectively. Table 1 shows the summary of simulation cases in this study.

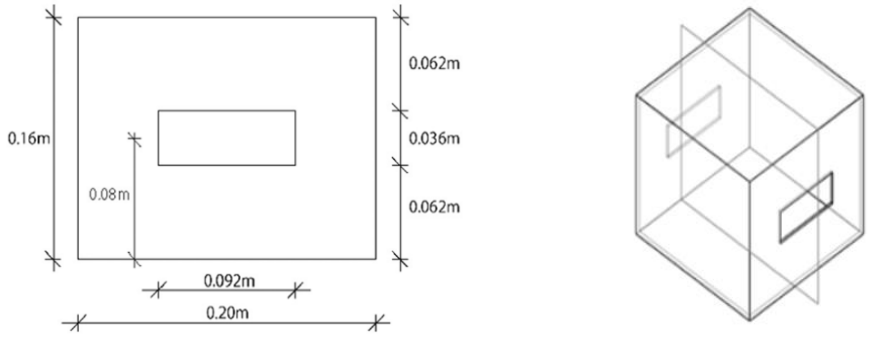

(a) (b)

Fig. 1 - (a) Dimensions in m and; (b) isometric view of the reference building model [17]

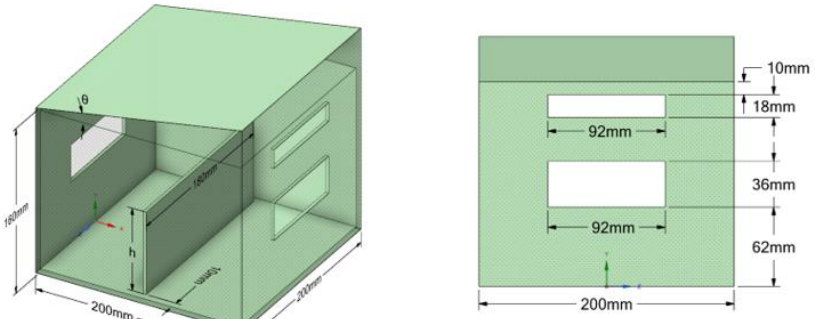

(a)

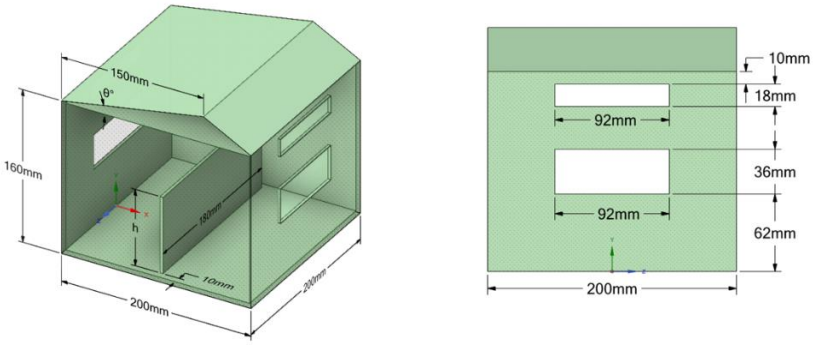

(b)

Fig. 2 - Dimensions for the (a) sawtooth roof and; (b) saltbox roof

2.2 Computational Domain

The selection of the computational domain size in this study was based on the the reference from van Hoff et al [17] and aligned with the contemporary practices [18]. The distance from the windward façade was set at 3H, while it was set at 15H from the leeward facade, and 5H from the top and sides, whereby H represents the reference building height of 160 mm. As a result, the dimension of computational domain is 3.08 m (L) × 1.80 m (W) × 0.96 m (H) as shown in Figure 3.

2.3 Boundary Conditions

The established boundary conditions were designed to replicate the wind tunnel test that was carried out previously. Initially, the mean streamwise velocity was fitted into the power law with an exponent of 0.25 using equation (1) [21]. Next, van Hooff et al recommended using the log law to obtain the $U^*_{ABL,}$ which is the atmospheric boundary layer friction velocity. Hence, the resulting log law equation is shown in equation (2) where z_0 = 0.0009m, κ is the von Karman constant of 0.42, and U^*_{ABL} = 0.348 m/s [21]. The turbulent kinetic energy, k was found by measuring the fluctuation in velocity by using equation (3). Then, the turbulent dissipation rate, ε was obtained by using equation (4) while the specific dissipation rate ω was obtained by using equation (5) whereby $C\mu$ was 0.09 [22].

$$\frac{U(z)}{U_H} = \left(\frac{z}{H}\right)^{0.25} \quad (1)$$

$$U(z) = \frac{u*_{ABL}}{\kappa} \ln\left(\frac{z + z_0}{z_0}\right) \quad (2)$$

$$\left(\frac{k(z)}{U_H{}^2}\right) = 0.033e^{-0.32\left(\frac{z}{H}\right)} \quad (3)$$

$$\varepsilon = \frac{(u*)^3}{\kappa(z + z_0)} \quad (4)$$

$$\omega = \frac{\varepsilon}{C\mu k} \quad (5)$$

Furthermore, the inlet plane was defined as the velocity vector while the outlet plane was defined as pressure outlet. Symmetry type was also applied to top and side wall of the domain. Next, the sand grain roughness Ks was applied to the ground surface and set to zero (Ks = 0) to replicate the smooth turntable.

Table 1 - Summary of the simulation cases

Roof Angle	Obstacle Height (h)	Roof Type
10°	none	Sawtooth roof and Saltbox roof
	80 mm	
	100 mm	
	120 mm	
	140 mm	
20°	none	
	80 mm	
	100 mm	
	120 mm	
	140 mm	
30°	none	
	80 mm	
	100 mm	
	120 mm	
	140 mm	
40°	none	
	80 mm	
	100 mm	
	120 mm	
	140 mm	

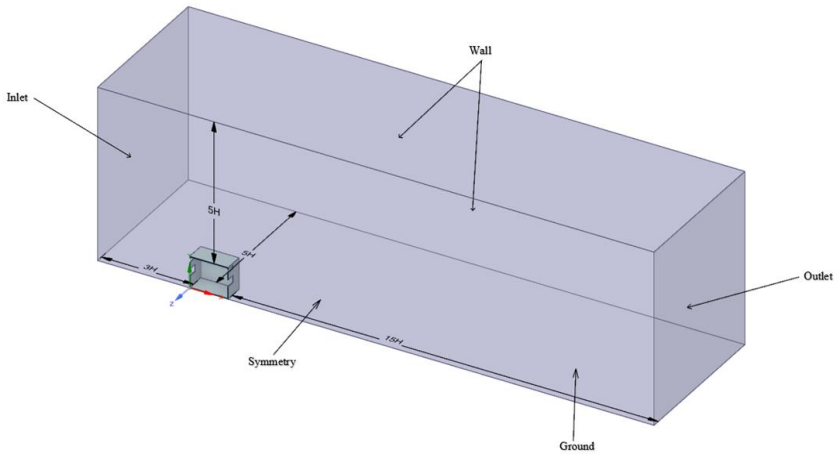

Fig. 3 - Dimensions of the computational domain

2.4 Solver Setting

In this research, all simulations were executed by using the ANSYS 2021 R2. The 3D steady RANS equation was solved with two turbulence models which was the Standard k-epsilon (SKE) and Shear Stress Transport (SST) k-ω model. Enhanced wall treatment (EWT) was used for both the turbulence models. Following the simulations, the results obtained from these turbulence models were compared against experimental data collected through wind tunnel testing. This comparison was to discern the turbulence model that best approximated experimental results. It is noteworthy that the simulations were considered successful upon reaching convergence, a state achieved when the residuals met predefined thresholds. Specifically, the convergence criteria were set at 10^{-6} for x, y, and z velocities, 10^{-5} for variables k (turbulent kinetic energy), ω (specific dissipation rate), and ε (turbulent dissipation rate), and 10^{-4} for continuity.

2.5 Grid Sensitivity Analysis

In order to acquire an accurate result, the grid sensitivity analysis was conducted to verify that the simulation result produced is independent of the grid size. The grid sensitivity analysis was carried out using the SST k-ω model. Three distinct grid sizes were generated namely course, medium and fine. The cell counts for the course, medium and fine grid were 1,332,961 cells, 1,867,187 cells, and 2,907,070 cells, respectively. The grid convergence index (GCI) shown in equation (6) was then used to calculate the error of the U/Uref value for the coarse and medium grids versus the fine grid [23]. The safety factor (SF) was taken as 1.25 as 3 grids are considered. Other than that, the grid refinement factor (r) of $\sqrt{2}$ was deployed, and the formal order of accuracy (p) was set to 2, given that the second-order discretization schemes were utilized.

$$GCI = SF \left| \frac{r^p \frac{U_{course} - U_{fine}}{U_{ref}}}{r^p - 1} \right| \quad (6)$$

Next, three vertical lines (x/D) were constructed at 0.125, 0.5 and 0.875. The GCI were calculated and averaged to determine the most optimal grid size. The x/D refers to ratio of the distance of vertical lines constructed to the total length of the building. The average GCI along the vertical lines of x/D = 0.125, 0.5 and 0.875 was 1.3173%, 2.8414%, and 1.2277%, respectively, for the coarse grid. Subsequently, the average GCI along the vertical lines for the medium grid of x/D = 0.125, 0.5 and 0.875 was 1.0892 %, 1.2877 %, and 0.5293%, respectively. Finally, the average GCI for course grid was found to be 1.7955% while the medium grid was 0.9687%. Therefore, the medium grid was selected for subsequent simulations because its results closely approximated those of the fine mesh, providing a nearly grid independent result. Figure 4 shows the comparison of U/Uref for three different grids.

2.6 Modal Validation

A model validation in accordance to the van Hoff et al model [17] was carried out to improve the reliability of the results. The factor of two of observation (FAC2) was used as a quantitative metric for model validation. FAC2 was used in this study as it is a robust validation method to analyse irregular occurring low or high observations and predictions within a specific dataset. The FAC2 equation is described in equation (7) below,

$$FAC\ 2 = \frac{1}{n}\sum_{i=1}^{n} N_i$$

$$where, N_i = \begin{cases} 1 & if\ 0.5 \leq \frac{P_i}{O_i} \leq 2 \\ 0; & else \end{cases} \quad (7)$$

whereby Pi is the predicted value generated from this study while Oi is the experimental result from wind tunnel experiment **Error! Reference source not found.**. If the observed value falls below or exceeds the compared value but remains within the predefined lower or upper threshold, it is regarded as an acceptable value. The indication for an ideal FAC2 value is 1. The average FAC2 was 0.72 for the SKE turbulence model while the SST k-ω had an average of 0.53 when compared to the wind tunnel experimental result. The SKE outperformed the SST k-ω turbulence model in terms of the FAC2 analysis. Since the SKE was found to be closest to the wind tunnel experimental result, the SKE turbulence model was adopted for the rest of the study. Table 2 shows the summary of FAC2 at various location when compared to wind tunnel experimental result. Figure 5 shows the model validation for the simulation compared to the experimental result for locations (x/D) at 0.125, 0.25, 0.375, 0.5, 0.625, 0.75, and 0.875.

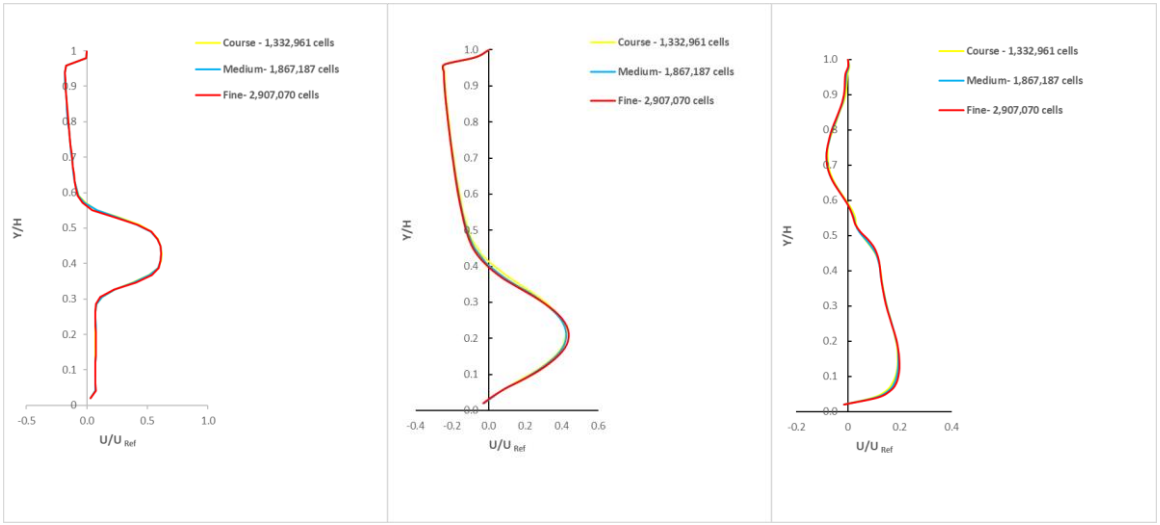

(a) (b) (c)

Fig. 4 - Comparison of U/Uref for three different grids at x/D of (a) 0.125; (b) 0. 5; (c) 0.875

Table 2 - FAC2 when compared to wind tunnel experimental result from van Hoff et al [17]

Location, x/D	FAC2	
	Medium Grid (Standard k-ε)	Medium Grid (SST k-ω)
0.125	0.78	0.69
0.25	0.73	0.49
0.375	0.69	0.54
0.5	0.73	0.5
0.625	0.70	0.46
0.75	0.68	0.43
0.875	0.73	0.6
Average	0.72	0.53

Next, to further verify the turbulence model chosen, the CFD results of dimensionless velocity from the simulations were also compared to the results from van Hoff et al [17]. The FAC2 quantitative metric was once again applied, yielding an average score of 0.78, signifying that approximately 78 percent of the data falls within the acceptable margin of error. Therefore, the turbulence model chosen (SKE) shows good agreement with the wind tunnel experimental result and simulation result from van Hoff et al [17]. Table 3 shows the summary of FAC2 at various location when compared to results obtained by van Hoff et al. Figure 6 shows model validation simulation compared to van Hoff for locations (x/D) at 0.125, 0.25, 0.375, 0.5, 0.625, 0.75, and 0.875.

Table 3 - FAC2 when compared to simulation result from van Hoff et al [17]

Location, x/D	FAC2
	Medium Grid (Standard k-ε)
0.125	0.90
0.25	0.77
0.375	0.79
0.5	0.76
0.625	0.70
0.75	0.73
0.875	0.84
Average	0.78

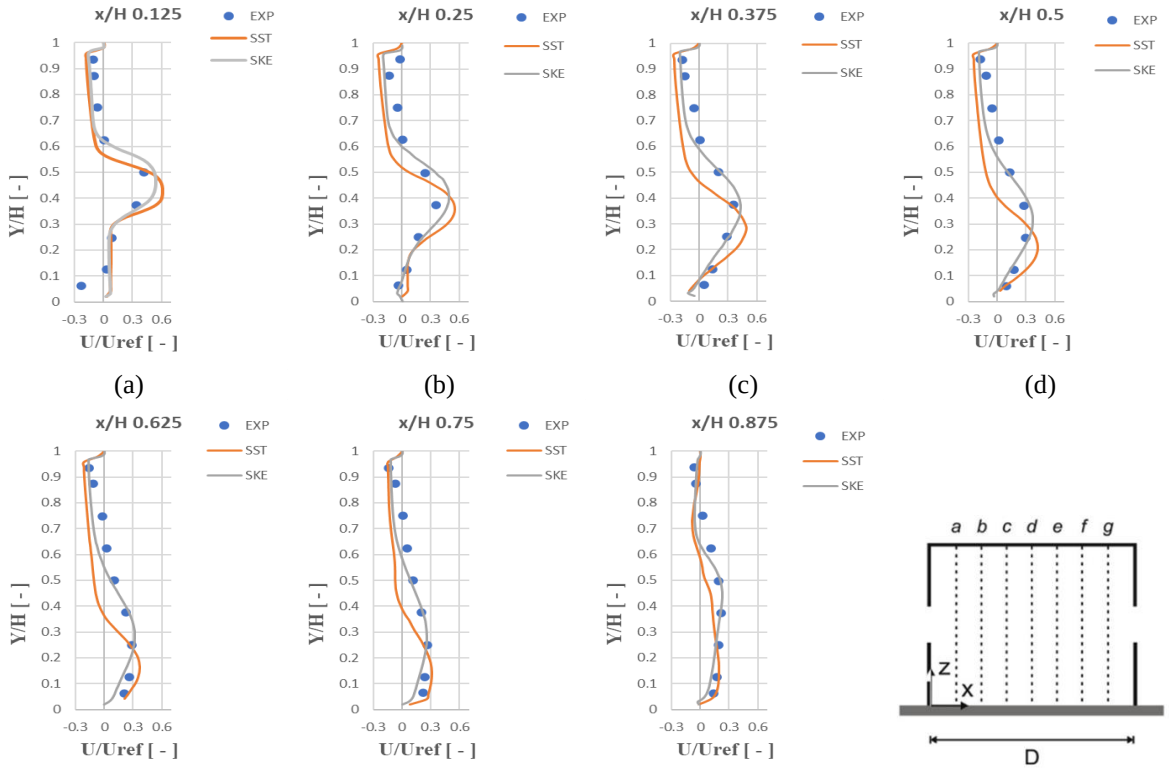

Fig. 5 - Model validation for the simulation compared to the experimental result from van Hoff et al [17] for locations (x/D) at (a) 0.125; (b) 0.25; (c) 0.375; (d) 0.5; (e) 0.625; (f) 0.75; (g) 0.875

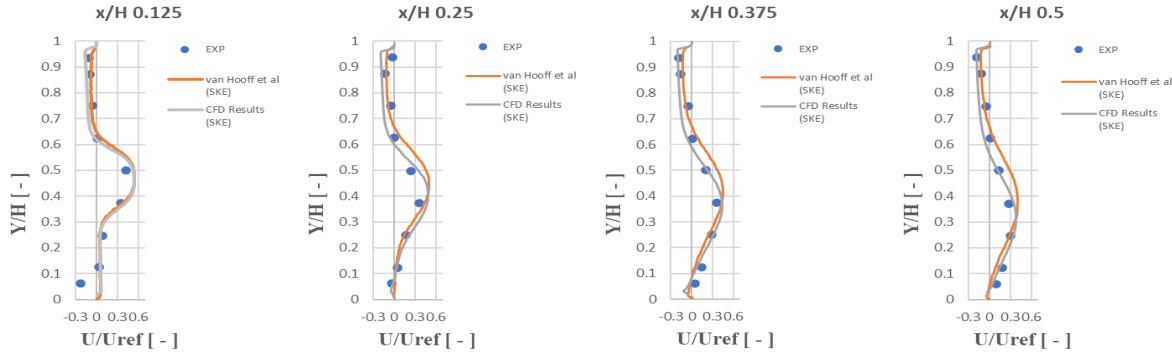

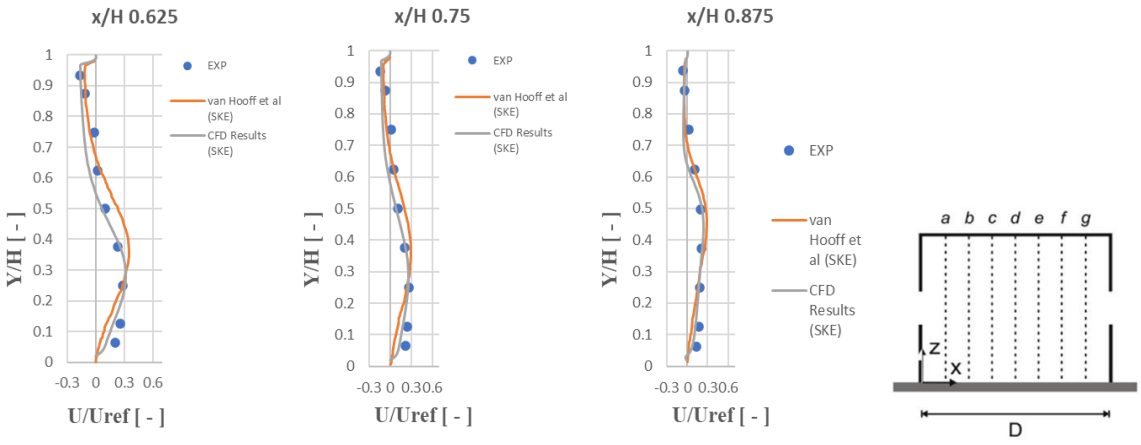

(e) (f) (g)

Fig. 6 - Model validation for the CFD results compared to simulations results from van Hoff et al [17] for locations (x/D) at (a) 0.125; (b) 0.25; (c) 0.375; (d) 0.5; (e) 0.625; (f) 0.75; (g) 0.875

3. Results and Discussion

3.1 Velocity Streamline

The impact of roof angle, roof shape, and internal obstacle on the airflow properties around the building is observed through the velocity streamline as shown in Tables 4 and 5. The recirculation region at the leeward roof grows larger as roof angle increases for both sawtooth and saltbox roof. As the roof angle increases, several notable phenomena become evident. Firstly, the centre of the recirculation eddy situated behind the roof elevates and moves away from the building. This observation aligns with findings from various studies focused on roof ventilation, where an increase in roof angle tends to magnify the recirculation zone, causing it to extend up to the roof ridge [5]. Next, flow separation is noticed at the windward corner of the building for 10° and 20° roof angle. On the other hand, when the roof angle increases, the air flow along the roof and flow separation occurs over the ridge of the roof. This can be attributed to the intensified impinging effect resulting from the higher roof angles, as elucidated in previous research [12]. On the other hand, reverse flow is not observed on the saltbox roof at 10°, however the reverse flow develops at 20° and grows larger in size with increment of roof angle. This finding is similar to results observed in various gable roof studies whereby reverse flow is present when a higher roof angle is used [5]. On the contrary, reverse flow is observed in sawtooth roof regardless of roof angle and the reverse flow grows with increment of roof angle. This shows that roof shapes have an effect on the external airflow property around the building. Subsequently, the increment of roof angle has a huge impact on internal airflow as well. The airflow in the window and roof opening is observed to increase in velocity as roof angle increases. The airflow entering through the window opening will be redirected downward as a result of both its specific opening location and the forming of a recirculation zone in front of the building [12]. Meanwhile, airflow entering from roof opening is observed to be deflected upwards and attached to the ceiling which is caused by the Coanda effect as seen in other study [24]. Next, the presence of an internal obstacle has been found to have a considerable influence on the building's internal airflow. When the airflow strikes the obstacle, a recirculation zone is formed in front of the obstacle. Consequently, when the obstacle height reaches 140 mm, a reverse flow is observed to occur at the leeward window opening. The reverse flow would reduce the velocity of the airflow leaving the building and cause the airflow to diverge as it exits the building.

Table 4 - Velocity streamline for sawtooth roof with various roof angle and obstacle height

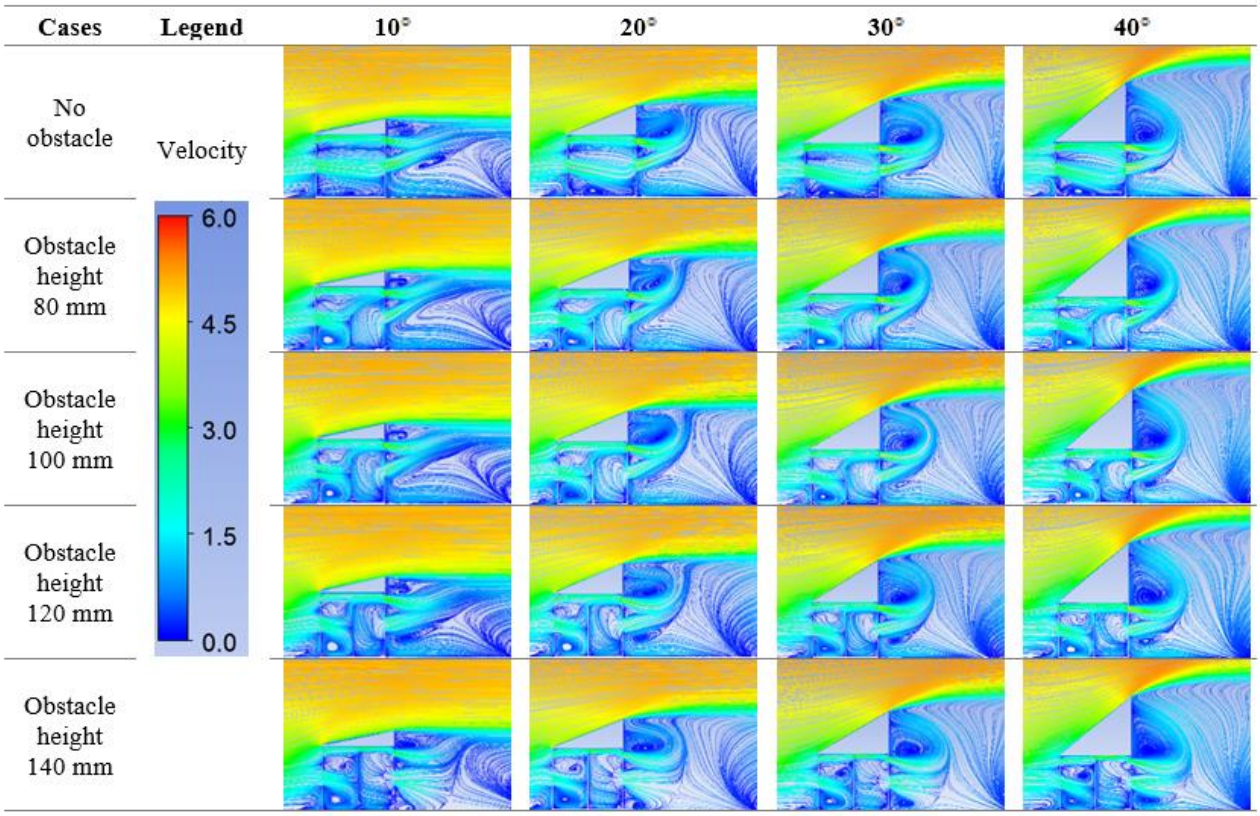

Table 5 - Velocity streamline for saltbox roof with various roof angle and obstacle height

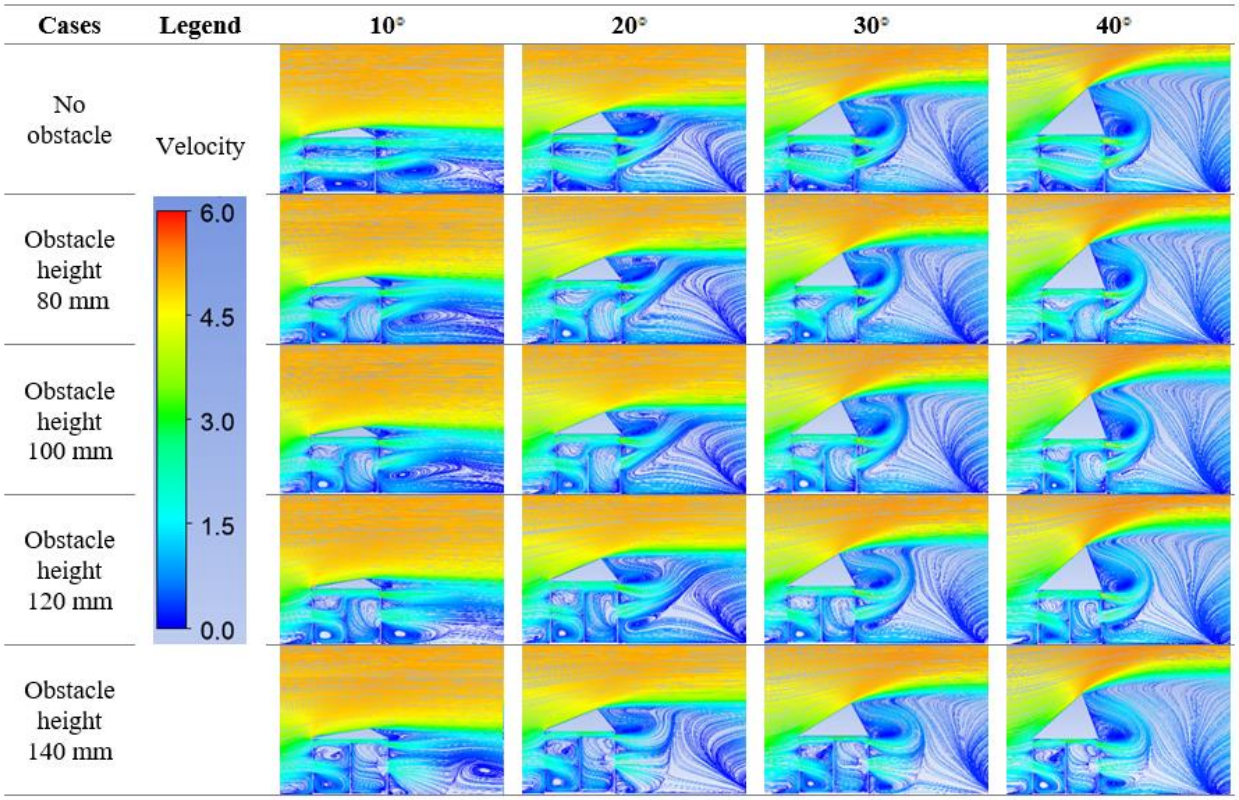

3.2 Spatial Distribution of Pressure Coefficient

Tables 6 and 7 show the spatial distribution of pressure for both roof configurations with different obstacle height. The pressure coefficient refers to spatial distributions of the static pressure around the building. Based on the results obtained in all cases, the highest C_p is observed to occur at the windward side of the building due to the effect of wind force on a wall [5]. Next in the case of 10° and 20° for both roof type, negative peak C_p is observed at the windward corner and the ridge of the roof. However, the negative peak will diminish and move towards the ridge of the roof. This is similar to results obtained from Tominaga et al due to the increment of roof angle which produces a larger building thus increasing the blockage towards the incoming air flow [7]. Additionally, with an increase in the roof angle, the magnitude of the negative pressure behind the structure also increases, primarily because of a more pronounced flow separation occurring at the roof ridge. Next, the presence of internal obstacle will change the spatial distribution of pressure inside the building. However, the spatial distribution of pressure outside the building is found independent of internal obstacle, which is consistent to the finding from the previous study [13]. Furthermore, the spatial distribution of pressure coefficient was found to be dependent on the roof shape. The sawtooth roof shape produces a greater negative peak throughout the leeward side while the saltbox roof produces the greater negative peak at the leeward roof ridge. A positive peak can be observed at the front of the obstacle due to the impact of the incoming wind from the windward opening. The positive peak is then observed to increase as the obstacle height increases due to more air being obstructed by a larger obstacle. Finally, for all the cases, as the roof angle increases, the internal pressure of the building also decreases due to higher wind speed. This demonstrates that the pressure distribution over the building has a significant correlation with wind speed which is in agreement with Bernoulli's principle.

3.3 Dimensionless Flowrate

The dimensionless flowrate (DFR) of the building is calculated by using equation (8), whereby Q is the volume flowrate through the building while the reference velocity is 4.3 m/s and the total area of window and roof opening is 0.004968 m^2

$$DFR = \frac{Q}{U_{ref} A_{inlet}} \tag{8}$$

Based on figures 7 and 8, the highest DFR for all cases is obtained for roof angle at 40°. The value of DFR also increases as the roof angle increases for both roof configurations. This is because the increase of roof angle will increase the wind speed entering the building as mentioned above.

Table 6 - Spatial distribution of pressure coefficient contours for sawtooth roof with various roof angle and obstacle height

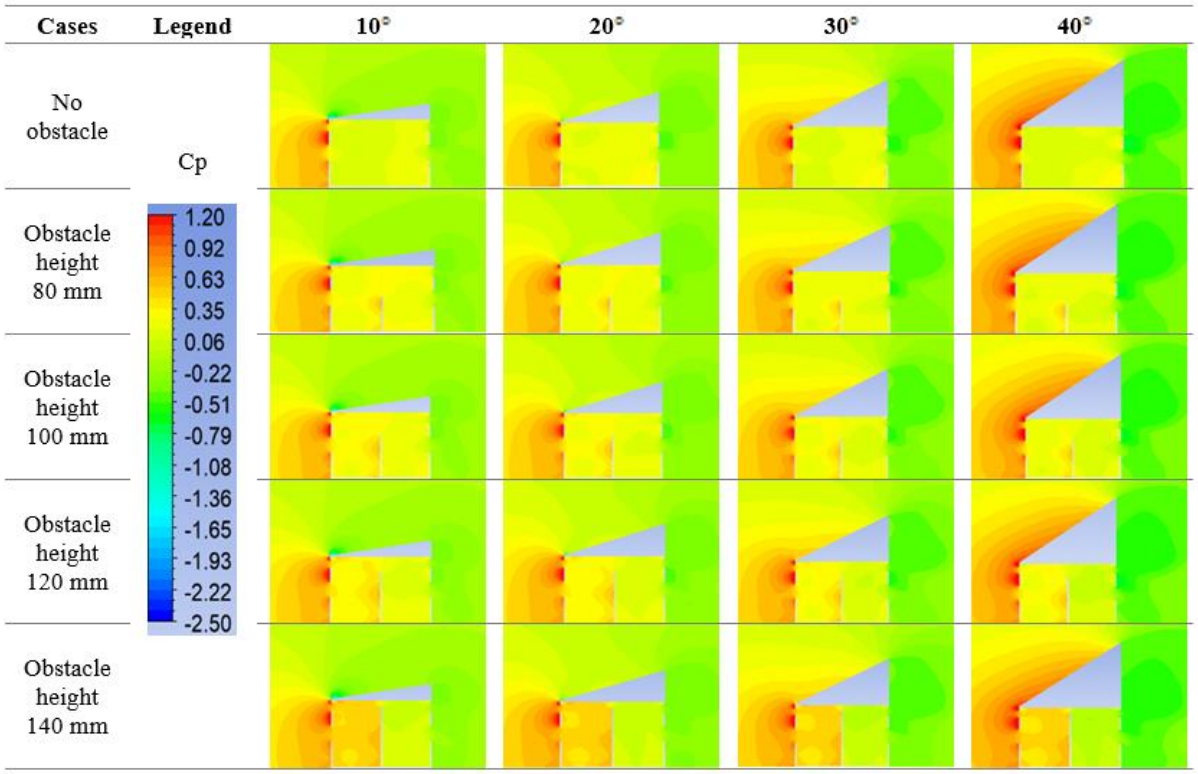

Table 7 - Spatial distribution of pressure coefficient contours for saltbox roof with various roof angle and obstacle height

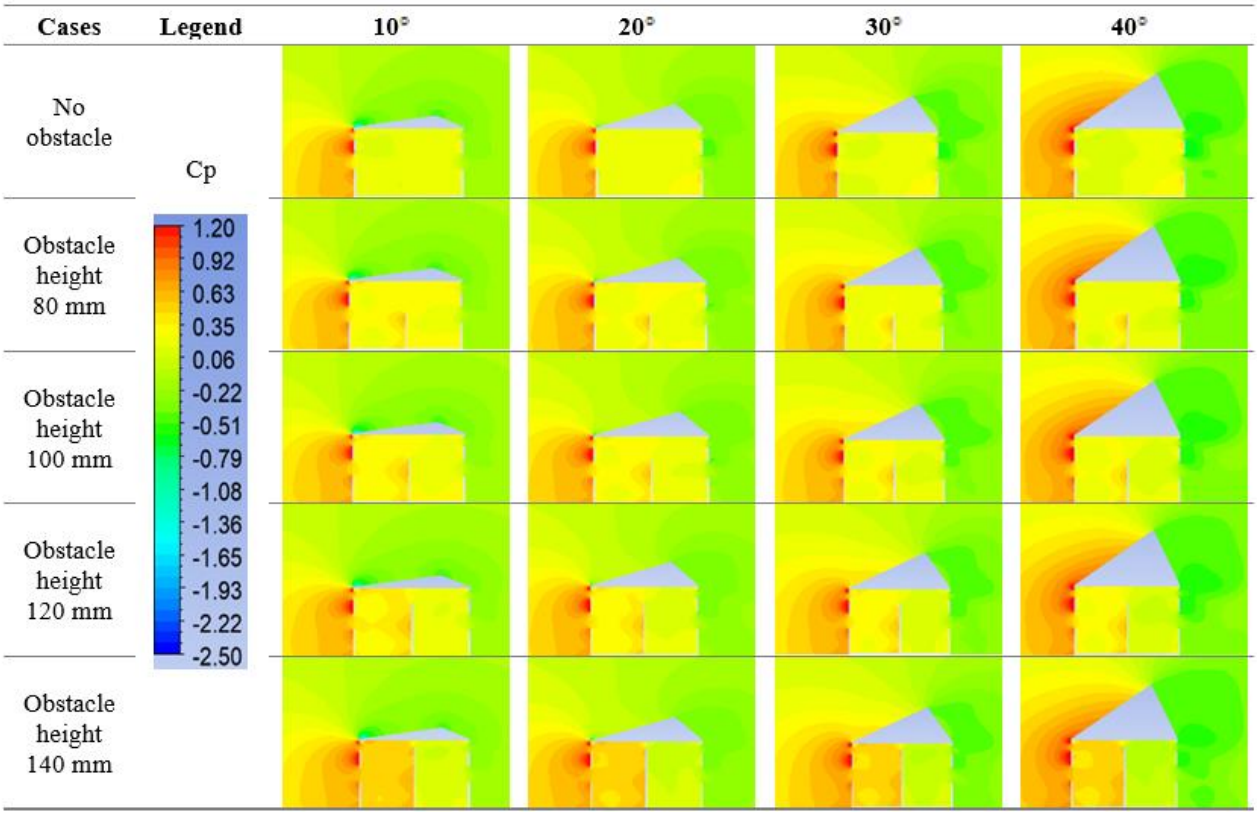

These findings are well in agreement with the previous studies whereby a higher roof angle usually provides a higher flowrate through the building thus increasing the ventilation rate [4]. Next, when similar roof angle and internal obstacle were used, the sawtooth roof was found to produce a slightly higher DFR when compared to the saltbox roof. Nevertheless, it should also be noted that even with the same roof angle, the sawtooth roof building is always taller than that of the saltbox roof. As a result, building height is another factor that influences the ventilation rate [4]. Other than that, the building with the presence of an internal obstacle will always have a lower DFR when compared to a building without an obstacle which is well in agreement with previous studies [15]. This is because the presence of an internal obstacle will block the incoming air. Additionally, the value of gradually DFR decreases as the obstacle height increases. This is because the larger internal obstacle will block more incoming air thus reducing air flow. Moreover, a substantial drop of DFR is observed when the internal obstacle height reaches 140 mm for all cases. This observation is well in agreement with a study conducted by Chu and Chiang whereby a reduction of ventilation rate of about 20% is observed when the blockage ratio is more than 75% [13]. The huge reduction in DFR can be attributed to the reverse flow at the leeward window opening obtained in the cases of 140 mm as discussed above.

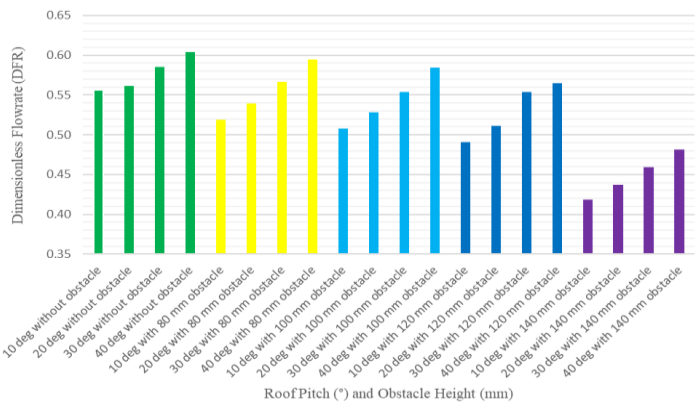

Fig. 7 - Dimensionless flowrate for the sawtooth roof with various roof angle and obstacle height

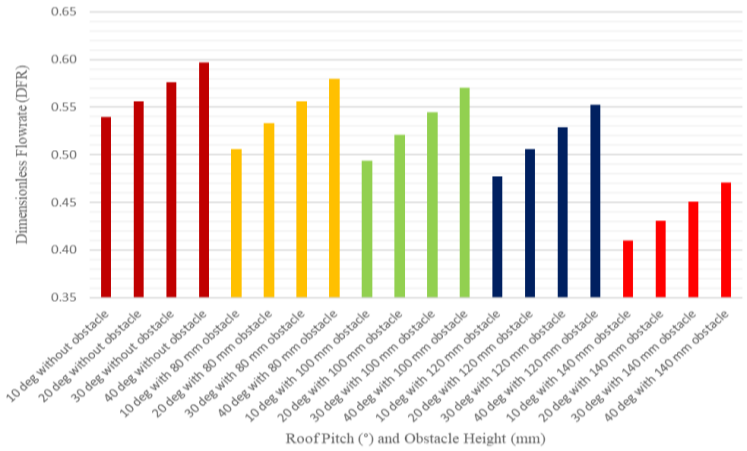

Fig. 8 - Dimensionless flowrate for the saltbox roof with various roof angle and obstacle height

4. Conclusion

Two different roof-configured buildings with various roof angles which are 10˚, 20˚, 30˚ and 40˚ were studied and analysed using CFD with steady-state 3D RANS simulations. Other than that, the buildings were added with various obstacle heights to analyse the effect of an internal obstacle in a natural-ventilated building. Next, the model validation shows well in agreement with the detailed numerical analysis and wind tunnel experiment conducted by previous researchers. Based on the results obtained, the airflow characteristics such as wind speed, pressure, and flowrate of an isolated building is influenced by the roof shape and roof angle. The flow separation caused by the ridge produced a larger recirculation zone behind the building as the roof angle increases. The reverse flow behind at the leeward side tends to grow bigger with increment of roof angle. Furthermore, the study revealed that the roof angle exerts a more significant influence on flow rate than the roof shape. Additionally, the presence of an internal obstacle results in the confinement of incoming air, leading to the formation of a high-pressure zone in front of the obstacle. As the size of the internal obstacle increases, the internal pressure within the building also rises. Moreover, the internal pressure within the building diminishes with increasing roof angles, attributed to the corresponding increase in wind speed. Next, DFR is measured to be highest with the largest roof angle while lowest with the smallest roof angle. Furthermore, the DFR of a building with internal obstacle is always lower than that without the presence of internal obstacle. In general, the sawtooth roof outperforms the saltbox roof in terms of the measured parameters. Additionally, the study shows that the roof angle and height of internal obstacle significantly influence the measured parameters compared to the roof shapes. In conclusion, the study found that the combination of sawtooth roof shape design, steeper roof angle, and without the presence of internal obstacle is able to produce the highest DFR through the building. To enhance the investigation of factors influencing naturally ventilated building, it is recommended for future research to incorporate different opening positions, angle of attack of incoming air flow and opening size with various roof configuration.

Acknowledgment

The authors fully acknowledged SEGi University and Teesside Universityfor supporting this work.

References

[1] Chao, Q., & Feng, A. (2018). Scientific basis of climate change and its response. Global Energy Interconnection, 1(4), 420-427.

[2] González-Lezcano, R., & Hormigos-Jiménez, S. (2016). Energy saving due to natural ventilation in housing blocks in Madrid. IOP Conference Series: Materials Science and Engineering, 138.

[3] Ibrahim, S. H., Roslan, Q., Affandi, R., Razali, A. W., Samat, Y. S., & Mohd Nawi, M. N. (2018). Study on the optimum roof type with 30° roof angle to enhance natural ventilation and air circulation of a passive design. International Journal of Technology, 9(8), 1692-1701.

[4] Perén, J. I., van Hooff, T., Leite, B. C. C., & Blocken, B. (2015). CFD analysis of cross-ventilation of a generic isolated building with asymmetric opening positions: Impact of roof angle and opening location. Building and Environment, 85, 263-276.

[5] Al-Aghbari, O. H., Moey, L. K., Tai, V. C., Go, T. F., & Yazdi, M. H. (2022). Study on the impact of sawtooth roof inclination angles and asymmetrical opening positions for an isolated building in cross ventilation. Jordan Journal of Mechanical & Industrial Engineering, 16(5), 865-878.

[6] Moey, L. K., Kong, M. F., Tai, V. C., Go, T. F., & Adam, N. M. (2021). Effect of gable roof angle on natural ventilation for an isolated building. Jordan Journal of Mechanical and Industrial Engineering, 15(3), 291-300.

[7] Tominaga, Y., Akabayashi, S. ichi, Kitahara, T., & Arinami, Y. (2015). Air flow around isolated gable-roof buildings with different roof pitches: Wind tunnel experiments and CFD simulations. Building and Environment, 84, 204-213.
[8] Mahdavinejad, M., & Javanroodi, K. (2016). Impact of roof shape on air pressure, wind flow and indoor temperature of residential buildings. International Journal of Sustainable Building Technology and Urban Development, 7(2), 87-103.
[9] Ameer, S. A., Chaudhry, H. N., & Agha, A. (2016). Influence of roof topology on the air distribution and ventilation effectiveness of wind towers. Energy and Buildings, 130, 733-746.
[10] Perén, J. I., van Hooff, T., Ramponi, R., Blocken, B., & Leite, B. C. C. (2015). Impact of roof geometry of an isolated leeward sawtooth roof building on cross-ventilation: Straight, concave, hybrid or convex? Journal of Wind Engineering and Industrial Aerodynamics, 145, 102-114.
[11] Liu, Z., Yu, Z., Chen, X., Cao, R., & Zhu, F. (2020). An investigation on external airflow around low-rise building with various roof types: PIV measurements and LES simulations. Building and Environment, 169, 106583.
[12] Moey, L. K., Kong, M. F., Tai, V. C., Go, T. F., & Adam, N. M. (2021). Effects of roof configuration on natural ventilation for an isolated building. Journal of Mechanical Engineering and Sciences, 15(3), 8379-8389.
[13] Moey, L. K., Cheong, S. K., Al Zobaied, M. A., Tai, V. C., Go, T. F., & Chong, P. L. (2023). Impact of eave and roof pitch on cross ventilation for an isolated building with sawtooth roof. Journal of Mechanical Engineering and Sciences, 17(2), 9474-9482.
[14] Chu, C. R., & Chiang, B. F. (2013). Wind-driven cross ventilation with internal obstacles. Energy and Buildings, 67, 201-209.
[15] Chu, C. R., Chiu, Y. H., & Wang, Y. W. (2010). An experimental study of wind-driven cross ventilation in partitioned buildings. Energy and Buildings, 42(5), 667-673.
[16] Zhang, X., Weerasuriya, A. U., Wang, J., Li, C. Y., Chen, Z., Tse, K. T., & Hang, J. (2020). Cross-ventilation of a generic building with various configurations of external and internal openings. Building and Environment, 207, 108447.
[17] van Hooff, T., Blocken, B., & Tominaga, Y. (2017). On the accuracy of CFD simulations of cross-ventilation flows for a generic isolated building: Comparison of RANS, LES, and experiments. Building and Environment, 114, 148-165.
[18] Blocken, B. (2015). Computational Fluid Dynamics for urban physics: Importance, scales, possibilities, limitations and ten tips and tricks towards accurate and reliable simulations. Building and Environment, 91, 219-245.
[19] Franke, J., Hellsten, A., Schlünzen, H., & Carissimo, B. (2007). Best practice guideline for the CFD simulation of flows in the urban environment. COST Action, 44(May), 1-52.
[20] Tominaga, Y., Mochida, A., Yoshie, R., Kataoka, H., Nozu, T., Yoshikawa, M., & Shirasawa, T. (2008). AIJ guidelines for practical applications of CFD to pedestrian wind environment around buildings. Journal of Wind Engineering and Industrial Aerodynamics, 96(10-11), 1749-1761.
[21] Karava, P., Stathopoulos, T., & Athienitis, A. K. (2011). Airflow assessment in cross-ventilated buildings with operable façade elements. Building and Environment, 46(1), 266-279.
[22] Richards, P. J., & Hoxey, R. P. (1993). Appropriate boundary conditions for computational wind engineering models using the k-ε turbulence model. In Computational Wind Engineering, 1, 145-153.
[23] Roache, P. J. (1997). Quantification of uncertainty in computational fluid dynamics. Annual Review of Fluid Mechanics, 29(1), 123-160.
[24] Tominaga, Y., & Blocken, B. (2016). Wind tunnel analysis of flow and dispersion in cross-ventilated isolated buildings: Impact of opening positions. Journal of Wind Engineering and Industrial Aerodynamics, 155, 74-88.
[25] Kindangen, J., Krauss, G., & Depecker, P. (1997). Effects of roof shapes on wind-induced air motion inside buildings. Building and Environment, 32(1), 1-11.